



Cite this: DOI: 10.1039/c7nr01064h

## AuGd integrated nanoprobe for optical/MRI/CT triple-modal *in vivo* tumor imaging†

Chao Xu,<sup>a,b</sup> Yaling Wang,<sup>\*b</sup> Chunyu Zhang,<sup>b</sup> Yanwei Jia,<sup>c</sup> Yunjing Luo<sup>\*a</sup> and Xueyun Gao<sup>\*b</sup>

Multi-modal imaging agents are desirable for tumor diagnosis because they can provide more information on the tumor than single-modal imaging agents. However, most reported multi-modal imaging agents are dual-modal agents rather than tri-modal agents; therefore, detailed information on the tumor may still be insufficient when such imaging agents are used. To ameliorate this issue, we synthesized a tri-modal imaging agent, composed of gold cluster and gadolinium oxide integrated nanoparticles (denoted as AuGds) using bovine serum albumin (BSA) as the template *via* a bio-mineralization method. The AuGds exhibit red fluorescence at ~660 nm for optical imaging, strong X-ray absorption (around 700 HU) for CT imaging, and a high  $r_1$  value (~12.39 mM<sup>-1</sup> s<sup>-1</sup>) for MR imaging. After being chemically modified with folic acid (FA), the AuGds can specifically target folate receptors on KB tumor cells, and permit *in vivo* optical, MR, and CT imaging of xenografted tumors. By comparing these three imaging modalities, very clear structural and anatomical information on the *in vivo* tumor can be obtained. The AuGds show good biocompatibility, quick renal clearance, and do not induce normal tissue toxicity *in vivo*.

Received 13th February 2017,

Accepted 6th March 2017

DOI: 10.1039/c7nr01064h

rs.c.li/nanoscale

## 1. Introduction

In the past decade, the incidence and mortality of cancer have greatly increased.<sup>1</sup> Noninvasive imaging modalities play an important role in the diagnosis of cancer, including visualization of the abnormal state of the body and the monitoring of physiological activity at the target site.<sup>2</sup> Available imaging modalities include optical imaging, magnetic resonance imaging (MRI), computed tomography (CT), ultrasound (US), positron emission tomography (PET), and single photon emission computed tomography (SPECT).<sup>3</sup> Each imaging modality

has its own unique advantages and intrinsic limitations.<sup>4</sup> For example, CT has advantages in spatial resolution, and differentiation of different tissue densities, and allows three-dimensional visual reconstructions of tissue; however, it suffers from poor sensitivity, especially in soft tissues with limited density differences.<sup>5</sup> MR imaging is a non-invasive and powerful imaging technology able to realize multi-parameter imaging. It is free from ionizing radiation and good for soft tissue imaging, but its disadvantages include the expense and long scan time.<sup>6</sup> Optical imaging has a high temporal resolution and sensitivity, but suffers from limited spatial resolution and cannot provide 3D tissue details.<sup>7</sup> A single imaging modal may therefore be insufficient to obtain all of the required information at a disease site.<sup>3</sup> Multi-modal imaging with the combination of two or more imaging modalities<sup>8–10</sup> can overcome the hurdles of traditional diagnoses, and achieve reliable and accurate detection of disease sites.

Conventional contrast agents employed in CT and MR imaging usually focus on small molecular agents.<sup>11,12</sup> These have the disadvantages of the absence of specificity, short clearance times and renal toxicity.<sup>13</sup> Multifunctional nanoparticles have been used in different imaging fields because of their good biocompatibility, large specific surface characteristics, longer clearance time than small molecules, and the ease with which they can be modified. They are usually employed as contrast agents in live imaging.<sup>11,14,15</sup> The size of Au clusters reaches the Fermi wavelength (*i.e.* <1 nm), which endows Au clusters with Vis–NIR (visible–near infrared) fluo-

<sup>a</sup>College of Life Science and Bioengineering, Beijing University of Technology, 100124, China. E-mail: luoyj@bjut.edu.cn; Tel: +86-10-67391667

<sup>b</sup>Key Laboratory for Biomedical Effects of Nanomaterials and Nanosafety, Institute of High Energy Physics, Chinese Academy of Sciences, Beijing 100049, China. E-mail: wangyaling@ihep.ac.cn, gaoyx@ihep.ac.cn; Tel: +86-10-88236709

<sup>c</sup>State-Key Laboratory of Analog and Mixed-Signal VLSI, University of Macau, Macau, China

† Electronic supplementary information (ESI) available: Fig. S1: the TEM statistics for AuGd diameters; Fig. S2: (a) the high resolution-TEM images of the AuGds, (b) the lattice structure image of the typical AuGds. Fig. S3: the EDS spectral analyses of the AuGds; Fig. S4: the UV-vis absorption spectra of FA (black line), BSA (red line), FA-BSA solution (blue line), AuGds (green line) and FA-AuGds (magenta line) with the same protein concentration which is 0.52 mg ml<sup>-1</sup>; Fig. S5: time-dependent biodistribution profiles of FA-AuGds in KB-tumor bearing mice ( $n = 4$ ); Fig. S6: (a)  $T_1$ -weighted tumor MR images, at 7 T, of KB tumor-bearing mice at 0, 0.5, 1, 2, 4, and 6 h after the tail intravenous injection of FA-AuGds. The corresponding change of the Contrast-Noise Ratio (CNR) with the time for (b) region 1 and (c) region 2. See DOI: 10.1039/c7nr01064h

rescence properties.<sup>16–18</sup> Apart from their good biocompatibility, the characteristic of easy urinary excretion facilitates a fast renal clearance of the cluster materials, avoiding the accumulation of materials and the potential for long-term toxicity.<sup>19</sup> On the basis of these characteristics, some researchers have focused on the application of Au clusters in *in vivo* imaging of tumors, including dual-modal imaging.<sup>20–22</sup> In previous research, we used albumin-stabilized Au clusters to outline the anatomy of mouse kidneys on 2D and 3D CT imaging, and the results indicate that clear visualization of the renal collecting system and ureters could be achieved.<sup>23</sup> Recently, gadolinium oxide nanoparticles have attracted much attention<sup>24,25</sup> because of their comparable MR imaging ability and reduced toxicity compared with the small molecular Gd(III) contrast agents. The conjugation of gadolinium oxide with metal nanoclusters is a possible route for the construction of a triple-modal imaging agent;<sup>26</sup> however, complicated processes have hampered its popularity. It would appear sensible to synthesize Au–Gd integrated nanoparticles using albumin as the template in one step. This would be much simpler than chemical conjugation of gadolinium oxide or Gd-DTPA with Au nanoclusters.<sup>20</sup> A large quantity of functional groups in the exposed albumin coating on the surface of the composite nanoparticles is available for the following modification of target agents. To the best of our knowledge, no attempt to use Au cluster-gadolinium oxide integrated nanoparticles as optical/CT/MR triple-modal tumor targeting imaging probes has previously been reported.

In this study, we synthesized Au cluster and gadolinium oxide integrated nanoparticles (denoted as AuGds) *via* a biomineralization method in one-step (Scheme 1), with bovine serum albumin (BSA) being employed as a template. The resultant AuGds showed good stability, ultrasmall particle size ( $3.93 \pm 0.57$  nm), and good biocompatibility. The  $T_1$  relaxivity and X-ray absorption coefficients of AuGds were measured to evaluate the MRI and CT imaging potential. After functionalization with folic acid, the cellular uptake and toxicity of

FA-AuGds were evaluated. Finally, optical, MR, and CT imaging of nude mouse tumors was performed to assess the triple-modal imaging capability of the particles. This involved intravenous injection of AuGds into an animal model. The potential *in vivo* toxicity of the AuGds was also investigated.

## 2. Materials and methods

### 2.1 Materials

BSA (>98% purity, biotechnology grade) was purchased from Amresco. Chloroauric acid tetrahydrate ( $\text{HAuCl}_4 \cdot 4\text{H}_2\text{O}$ ), sodium hydroxide, folic acid (FA, 97% purity), *N*-hydroxysuccinimide (NHS), and *N*-(3-dimethylaminopropyl)-*N*'-ethylcarbodiimide hydrochloride (EDC) were all purchased from Sigma–Aldrich (St Louis, MO, USA). Gadolinium(III) chloride hexahydrate ( $\text{GdCl}_3 \cdot 6\text{H}_2\text{O}$ ) was purchased from Alfa Aesar (Tianjin, China). Ultrapure water ( $18.2 \text{ M}\Omega \text{ cm}$ ) was obtained from a Milli-Q synthesis system (Millipore, Billerica, MA, USA). Gadopentetic acid dimeglumine salt injection (Gd-DTPA, Magne-vist) was purchased from Bayer Schering Pharma AG (Germany).

### 2.2 Synthesis of AuGds

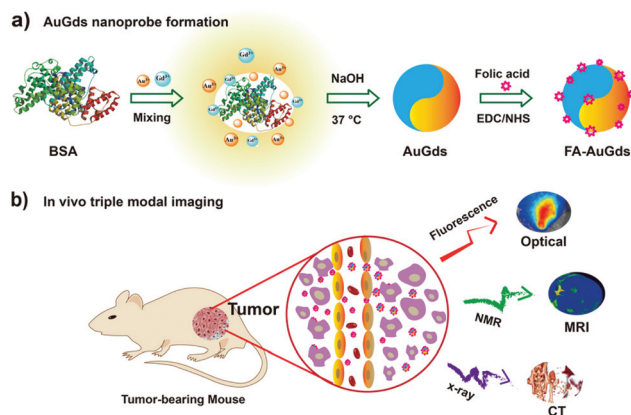
The AuGds were synthesized *via* a one-step method with BSA as a template. Briefly, the freshly prepared aqueous  $\text{HAuCl}_4$  (4 mL, 25 mM) and  $\text{GdCl}_3 \cdot 6\text{H}_2\text{O}$  (1 mL, 12.5, 25, 37.5, 50, 62.5, 75, 87.5, 100 mM) were premixed. The mixture was then injected into BSA (5 mL,  $50 \text{ mg mL}^{-1}$ ) solution under vigorous stirring at  $37^\circ \text{C}$  for 5 min. Following this, 1 mL of 2 M NaOH was added to the pre-blended solution and it was stirred for 12 h at  $37^\circ \text{C}$ . A dialysis tube (Merck, Midi D-tube, MWCO: 30 K) was used to remove other free ions. The fluorescence emission spectra were then recorded to find the optimal molar proportion of Au and Gd. The stability of AuGds obtained under the optimal reaction ratio was also investigated in a further experiment.

### 2.3 Functionalization of AuGds with FA

The AuGds were conjugated with FA using a zero-length cross-linker EDC and NHS. Briefly, FA solution ( $0.8 \text{ mL}$ ,  $44.14 \text{ mg mL}^{-1}$ ) was prepared with a 0.2 M NaOH deionized water solution, the pH of the FA solution was adjusted to 6.5–7.5, then EDC ( $0.2 \text{ mL}$ ,  $95.85 \text{ mg mL}^{-1}$ ) and NHS ( $0.2 \text{ mL}$ ,  $23.02 \text{ mg mL}^{-1}$ ) were added to the FA solution and the mixture was allowed to react for 4 h at ambient temperature. Finally, the previously prepared AuGds (10 mL), which were dialyzed against deionized water for 12 h, were put into the activated FA solution, and reacted for 6 h at ambient temperature. The as-prepared FA-AuGds were dialyzed against deionized water for 24 h (dialysis tube: MWCO 30 000), then stored at ambient temperature for future use.

### 2.4 Characterization

The morphology of the as-synthesized AuGds was investigated using high-resolution transmission electron microscopy



**Scheme 1** Schematic illustration of (a) the process of preparing AuGds, and (b) using them as imaging reagents for optical/MR/CT triple-modal tumor imaging *in vivo*.

(HRTEM; JEM-2100 transmission electron microscope, Japan). UV-vis absorption spectra of BSA and AuGds were recorded on a Shimadzu UV-1800 spectrophotometer (Japan). The fluorescence spectra of AuGds were measured on a Shimadzu RF-5301 fluorescence spectrophotometer. Elemental concentrations of Au and Gd were measured by inductively coupled plasma-mass spectrometry (ICP-MS). The chemical states of the elements constituting the AuGds were checked by X-ray photoelectron spectroscopy (XPS, Thermoescalab 250Xi) with a monochromatic 150 W Al K $\alpha$  X-ray source.

### 2.5 *In vitro* stability and cell target imaging of FA-AuGds

The stability of FA-AuGds dispersed in 10% fetal bovine serum (FBS) buffer solution was investigated by recording the fluorescence emission and absorption spectra at 0, 1, 2, 4, 12, and 24 h. To test the suitability of FA-AuGds as a candidate for *in vitro* fluorescence imaging, a known concentration of freshly prepared FA-AuGds (60  $\mu\text{M}$ ) was added to a confocal imaging glass-bottom dish containing KB cells (folate receptor positive) in a folic acid free 1640 medium or A549 cells (folate receptor negative) in a DMEM medium at a density of  $5 \times 10^5$  cells per well. The solution in the dish was removed after 4 h of incubation in 5% CO $_2$  at 37  $^\circ\text{C}$ , and the dish was washed three times with PBS to remove non-specific binding FA-AuGds. The lysosomes of cells were marked by using a green lysosome probe (Lysotracker@green DND-26, Invitrogen), and the cells were then washed with PBS to remove excess dye, and were fixed with 3.7% paraformaldehyde. The cells were imaged using an UltraVIEW Vox (PerkinElmer) confocal system attached to a Nikon Ti-e microscope with  $40 \times 1.4$  and  $60 \times 1.4$  NA plan apochromat oil immersion lenses. Excitation wavelengths were set at 488 nm (Lysotracker@green DND-26) and 561 nm (AuGds), and emission wavelengths were set to 520 nm (green) and 650 nm (red).

### 2.6 Cytotoxicity assay

The toxicity of the materials at different concentrations was investigated. Briefly, the cells were seeded at a density of  $1 \times 10^4$  cells per well in a 6-well plate with 10% FBS, and cultured overnight. They were then incubated with different concentrations of FA-AuGd solution for 24 h. The *in vitro* cytotoxicity assay was measured by staining with Live-Dead kits (Calcein-AM&PI, Dojindo Lab., Japan). The staining solutions, Calcein-AM and PI, were added to the 6-well plates giving final concentrations of 2  $\mu\text{mol l}^{-1}$  and 4  $\mu\text{mol l}^{-1}$ , respectively. Finally, the *in vitro* cytotoxicity results were measured and observed using a fluorescence microscope (20 $\times$  objective lens). For the cell viability assay, the cells were plated into 96-well plates (5000 cells per well) and pre-incubated for 24 h. The experimental cell groups were incubated with a series of concentrations of Au (0, 1, 2.5, 5, 10, 100, 250 and 500  $\mu\text{M}$ ) for 24 h or 48 h (each group having 5 parallel samples). The wells were then washed twice with PBS, and subsequently, 10  $\mu\text{l}$  of fresh Cell Counting Kit-8 (CCK-8, Dojindo Lab., Japan) solution was added to the culture medium and the cells were incubated for an additional 2 h. The absorbance of the samples was monitored at 450 nm

using a microplate reader (Spectra Max M2; Molecular Devices, Sunnyvale, USA). The cell viabilities relative to the control cells were calculated.

### 2.7 *In vitro* hemolysis assay

To evaluate the biocompatibility of AuGds *in vitro*, 1 ml of blood sample was obtained from mice and stabilized with 15% EDTA-K $_2$  solution. PBS (2 ml) was added to the solution and red blood cells were separated from the serum by centrifugation at 2000 rpm for 10 min, washed several times with PBS, and diluted to 10 ml with PBS. Then, 0.5 ml of diluted red blood cell (RBC) suspension was mixed with 0.5 ml AuGds at concentrations ranging from 0 to 1500  $\mu\text{g mL}^{-1}$ , with 0.5 ml PBS as a negative control and 0.5 ml deionized water as a positive control. The mixtures were then lightly shaken in an orbital shaker for 3 h at room temperature, before centrifugation at 10 050 rpm  $\text{min}^{-1}$  for 3 min. The absorbance of the supernatants was measured at 570 nm by using a UV-vis spectrophotometer. The percentage hemolysis was calculated with the following equation: hemolysis percent (%) =  $(A_{\text{sample}} - A_{\text{negative}})/(A_{\text{positive}} - A_{\text{sample}}) \times 100\%$ , where  $A_{\text{positive}}$ ,  $A_{\text{negative}}$ , and  $A_{\text{sample}}$  are the absorbance of the positive control, negative control, and sample, respectively.

### 2.8 Fluorescence imaging and distribution study

Female BALB/c-nu nude mice of 4 weeks of age were purchased from Beijing HFk bioscience CO., LTD (Beijing, China) and used under protocols approved by Key Laboratory for Biomedical Effects of Nanomaterials and Nanosafety (Institute of High Energy Physics, CAS). A xenografted tumor model was established by subcutaneous injection of  $1 \times 10^7$  cells into each nude mouse. *In vivo* tumor targeted optical imaging was performed when the tumors reached 8  $\times$  8 mm. And these tumor-bearing mice were used in subsequent animal assays, unless otherwise noted. Every three mice with similar tumor volumes were divided into groups. And the experiments were performed in triplicate.

Aliquots of 200  $\mu\text{l}$  of saline (control), AuGds, and FA-AuGd saline solutions (concentration of Au elements = 11.4 mM) were intravenously injected into mice through tail veins. After treatment, mice were gas anesthetized using isoflurane and imaged at 4 h post-injection. Optical imaging of the whole body and dissected organs was performed using a CRI Maestro *in vivo* imaging system equipped with an excitation band pass filter at 605 nm, with emission at 645 nm. At the end of the whole body imaging, the mice were sacrificed by cervical dislocation, and the tumor, heart, liver, spleen, lungs, and kidneys were collected and immediately imaged. The fluorescence intensity of different organs was analyzed using Maestro 2 software.

### 2.9 The $r_1$ relaxivity measurement and $T_1$ -weighted MRI *in vivo*

The  $r_1$  value and MR imaging of different concentrations of AuGds with Gd element concentrations of 0.031, 0.062, 0.125, 0.25, 0.5 and 1 mM were investigated, and compared with Gd-

DPTA. The phantom MR images were taken on a 7-Tesla micro-MRI Scanner (BioSpec70/20USR, Bruker) at room temperature. The following imaging parameters were used:  $T_1$ -weighted RARE sequence, TR: 300 ms, TE: 6.06 ms. The relaxation time was measured using the map\_MSEM sequence with various  $T_1$  values (TR: 230, 500, 1000, 1500, 3000 ms, TE: 6.06 ms), and signal intensity was recorded using a region-of-interest (ROI) for each sample after acquiring the MR images.

To confirm the  $T_1$  contrast ability of FA-AuGds, they were injected into mice *via* the tail vein (200  $\mu$ l, Au = 11.4 mM). Each experimental group has 4 mice. The images of the tumor sites were taken at different time-points post-injection (0, 0.5, 1, 2, 4, and 6 h) on the 7-T MRI scanner using the following parameters:  $T_1$ -weighted sequence, TR: 500 ms, TE: 8 ms, flip angle = 144.4°, matrix = 256  $\times$  256, FOV = 3.0  $\times$  3.0 cm, slice thickness = 1 mm. For future investigation of the tumor site and obtain clear information, the images were processed with the syngo Fast Explorer software, and converted to the spectrum 16 image form. To quantitatively evaluate the changes in the tumor site, two specific regions were chosen for contrast-to-noise ratio (CNR) analysis.

### 2.10 Hounsfield unit (HU) values and *in vivo* CT imaging

The physical properties of FA-AuGds as CT imaging reagents were investigated. Solutions of AuGds and BSA-Au NCs at various concentrations of the Au element were prepared in de-ionized water in different 1.5 ml tubes for a phantom test. The CT values of different Au element concentrations were measured and compared with the CT value of iopromide.

For *in vivo* CT imaging, FA-AuGds were injected into mice *via* the tail vein (200  $\mu$ l, Au = 11.4 mM), and 20  $\mu$ l of FA-AuGds were injected directly into the tumor. The mice ( $n = 4$ ) were then anesthetized and subjected to CT imaging using a SPECT/CT scanning system at 4 h and 0.5 h post-injection.

### 2.11 Toxicity test in mice

The toxicological effects of the FA-AuGds and AuGds on mice organs were evaluated by monitoring histological changes in several related organs. After intravenous administration of FA-AuGds and AuGds (200  $\mu$ L, 0.5 mmol Au per kg mice), adult athymic BALB/c mice ( $n = 3$ ) were dissected at 7 days, and related organs were removed. These were stained with hematoxylin and eosin (H&E) before investigation of tissue damage to the organs.

## 3. Results and discussion

### 3.1 Synthesis, characterization and stability

The molar ratio of Au to Gd is critical to fluorescence intensity, CT and MR contrast, and the stability of the resultant imaging agent. A series of ratios of Au<sup>3+</sup> to Gd<sup>3+</sup> ions were studied to optimise the optical properties and stability.

Fig. 1a and b show the digital images and fluorescence spectra of different ratios of Au to Gd. There is no obvious change in the fluorescence images under UV lamp excitation,

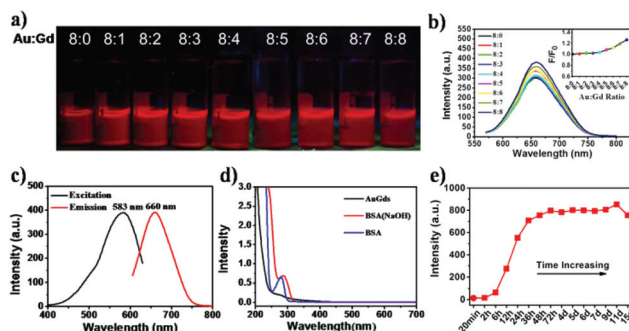


**Fig. 1** (a) The fluorescence images and (b) the corresponding fluorescence spectra of AuGds at different molar ratios of Au to Gd. (c) The fluorescence spectra of AuGds obtained at the optimal Au/Gd ratio. Black curve: the excitation spectrum of AuGds. Red curve: the emission spectrum of AuGds. (d) The UV-vis absorption spectra of AuGds (black line), BSA with NaOH solution (red line), and BSA solution (blue line). (e) The fluorescence intensity changes of AuGds at 660 nm against time.

although the maximum emission intensity increased with the ratio of Au/Gd. This implies that the higher the Gd concentrations used, the stronger the fluorescence of AuGds. However, when the ratio is over 8 : 4, the stability of the resulting AuGds decreases with storage time. Therefore, 8 : 4 was chosen as the optimal reaction ratio for AuGd synthesis. The fluorescence spectra of the resulting AuGds are shown in Fig. 1c. The maximum excitation and emission peaks are located at 583 and 660 nm, respectively. From Fig. 1d, it can be seen that the BSA solution has an absorption peak at 290 nm, which is attributed to the aromatic amine acid.<sup>27</sup> A red shift was observed when the NaOH solution was introduced into the BSA solution; this was attributed to the loss of a proton from the phenolic hydroxyl. The proton loss from the phenolic hydroxyl leads to an increase in the conjugation effect, which results in a red shift of the absorption peak.<sup>28</sup> The BSA specific absorption peak disappears while a shoulder peak appears. This results from a redox reaction of the aromatic amine acid. The maximum fluorescence emission peaks were recorded over 10 days, and Fig. 1e demonstrates that the AuGds were very stable at room temperature, with no significant change being observed after the plateau was reached.

The sizes and morphology of AuGds were characterized by HRTEM. As Fig. 2a shows, the particles are well dispersed, with a sphere-like geometry, and a mean diameter of  $3.93 \pm 0.57$  nm. Crystal structure analysis showed that the Au cluster mixed with the gadolinium oxide nanoparticles formed integrated nanoparticles. The high-resolution TEM (HR-TEM) image (ESI Fig. S2†) shows clear lattice fringes of 0.226 nm ascribed to the (102) facet of the hexagonal Gd<sub>2</sub>O<sub>3</sub> crystal, and 0.203 nm and 0.144 nm ascribed to the (200) and (220) facet of the cubic Au crystal, respectively. Energy dispersive spectroscopy (EDS) data confirmed the atomic ratio of Au : Gd as 2 : 1 (ESI S3†), which is in good accord with the ingredient proportion. To probe the detailed electron structure of the AuGds, the X-ray photoelectron spectroscopy (XPS) spectra of Au 4f, Gd 4d and S 2p were measured (Fig. 2b–d). The Au 4f<sub>7/2</sub> binding

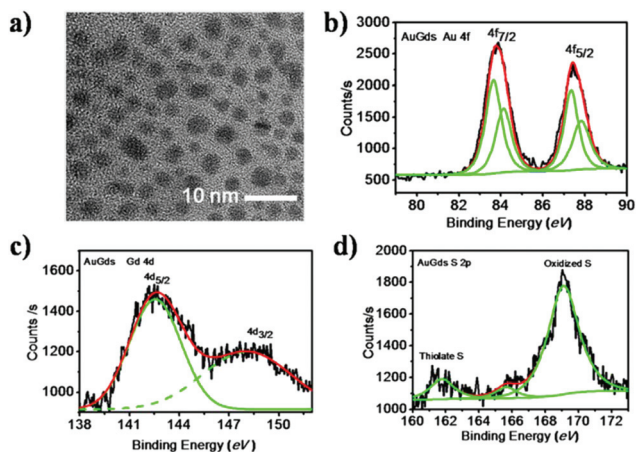


**Fig. 2** (a) TEM images of resulting AuGds with an average diameter of  $3.93 \pm 0.57$  nm (the histogram of size distributions is shown in ESI S1†). (b–d) XPS spectra of Au 4f, Gd 4d and S 2p for AuGds, respectively. Black curve, raw experimental data; red curve, data fitted curve; green curves, the data analyzed by using XPS software.

energy attributed to Au (0) emerged at 83.64 eV and the  $4f_{5/2}$  binding energy emerged at 87.34 eV. The Au  $4f_{7/2}$  binding energy attributed to Au(I) emerged at 84.12 eV and the  $4f_{5/2}$  binding energy emerged at 87.82 eV. The Au(I) was reported to be formed from the thiol-Au(I) binding on the outermost layer of the Au core, and this stabilizes the NCs, permitting the charge transfer from the ligand to the metal.<sup>27,29</sup> The Gd  $4d_{5/2}$  binding energy emerged at 142.5 eV, corresponding to the Gd element binding energy of  $Gd_2O_3$ .<sup>30,31</sup> Moreover, the binding energy of S  $2p_{3/2}$  was 169.1 eV, which corresponds to the binding energy of the sulfur to gold bond.

### 3.2 *In vitro* stability and cell targeted imaging of FA-AuGds

Prior to biological application, FA was conjugated with the AuGds to increase the tumor targeting ability (ESI Fig. S4†). To evaluate the efficiency of the grafted FA on the AuGd probe, we performed the UV-vis absorption spectroscopy of FA, BSA, FA-BSA, AuGds, and FA-AuGds with the same BSA protein concentration which is  $0.52 \text{ mg ml}^{-1}$ . As ESI Fig. S4† shows, the characteristic shoulder of FA (around  $\lambda = 363 \text{ nm}$ ) in the UV-vis absorption spectrum appeared after BSA and AuGds were modified with FA.<sup>32</sup> The stability of the FA-AuGds in 10% fetal

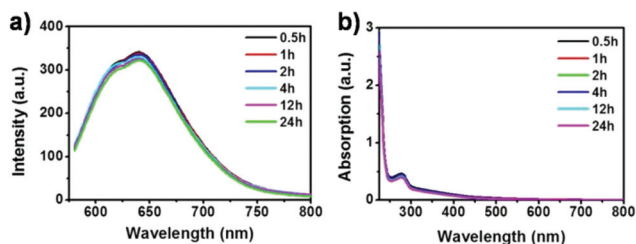


**Fig. 3** Stability of FA-AuGds tested by dispersion in 10% FBS buffer solution and recording time-dependent (a) fluorescence emission, and (b) optical absorption.

bovine serum (FBS) buffer solution was therefore investigated, and results are shown in Fig. 3. The fluorescence intensity of FA-AuGds did not obviously decrease, and the UV-vis spectral analysis showed no obvious surface plasmon resonance (SPR) absorption, indicating that the materials did not obviously aggregate. This suggests that the FA-AuGds in 10% FBS buffer are stable over 24 h.

To demonstrate the targeting ability of the FA-AuGds, two kinds of cells, KB and A549, were employed for targeted cell imaging. The KB cells overexpress the folate receptor. However, the A549 cells do not express the folate receptor, and could thus be employed as a negative control.<sup>33,34</sup> We expected that the FA-AuGds would effectively target and incorporate into the KB cells *via* receptor-mediated endocytosis, as FA can bind to folate receptors, which are expressed at high levels in KB cells. Fig. 4a and b show the respective confocal micrographs of KB and A549 cells after incubation with FA-AuGds for 4 h. The results indicate that FA-modified nanoparticles successfully entered into KB cells, and lysosome probe co-localization revealed the FA-AuGds accumulated in lysosomes within 4 h. In contrast, the fluorescence intensity was much weaker in A549 cells, even though the AuGds were modified with FA. These results suggest a high specificity of the FA-AuGds.

### 3.3 Evaluation of material cytotoxicity and *in vitro* hemolysis assay

For further biomedical applications, it is necessary to understand the cytotoxicity of these FA-AuGds. The cells were incubated with a series of concentrations of FA-AuGds (Au element concentration: 0, 50, 100, 200, 400 and 800  $\mu\text{M}$ ) for 24 h. A set of wells were also left unexposed to any samples to act as controls. Live-Dead staining was performed to evaluate the cytotoxic effects on KB cells after incubation with the sample for 24 h (Fig. 5a). No significant cell apoptosis was found within 24 h when incubation was performed with concentrations of FA-AuGds from 0 to 800  $\mu\text{M}$ . Meanwhile, to quantitatively evaluate the cytotoxicity of FA-AuGds, we performed a CCK-8 assay to evaluate the cell viability of KB cells after incubation with FA-AuGds for 24 and 48 h (each group had 5 parallel

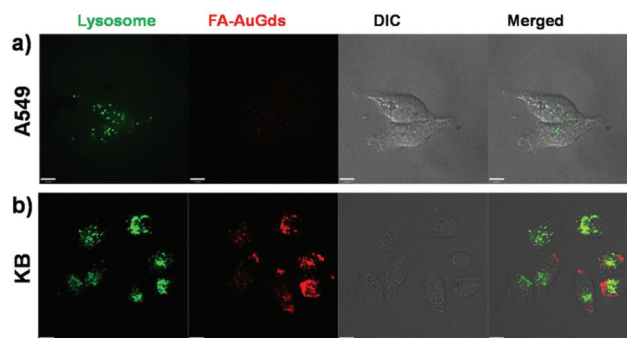


**Fig. 4** Confocal fluorescence images of (a) A549 cells and (b) KB cells cultured with FA-AuGds for 4 h in folate-free medium. Green fluorescence shows the lysosome probe fluorescence, and red fluorescence shows the FA-AuGd fluorescence.

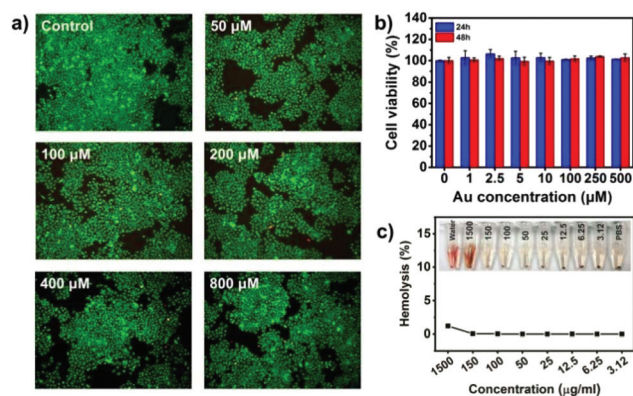


**Fig. 5** (a) Live–Dead staining of KB cells. KB cells were incubated with different concentrations of FA-AuGds for 24 h. (b) Cell viability of KB cell lines treated with a series of concentrations of FA-AuGds for 24 and 48 h, respectively. Each column represents the mean value ( $N = 6$ ) ( $p < 0.05$ ). (c) *In vitro* hemolysis assay. Percentage of hemolytic RBCs incubated with FA-AuGds at various concentrations for 3 h, using deionized water (+) and PBS (–) as positive and negative controls, respectively. Inset: photographs of direct observations of hemolysis, suggesting that FA-AuGds exhibit good biocompatibility.

samples; Fig. 5b). The FA-AuGds did not cause cell toxicity. The viability remained 100% after treatment with various concentrations of FA-AuGds, even when the concentration of samples reached 500 μM of Au (250 μM of Gd). The results indicate that FA-AuGds have low cytotoxicity to KB cells.

Additionally, we investigated the influence of AuGds on the hemolysis of red blood cells to evaluate their biocompatibility. We found negligible hemolysis of red blood cells, even when the incubation concentrations of AuGds were up to 1500 μg ml<sup>-1</sup>, indicating that FA-AuGds possess admirable blood compatibility (Fig. 5c). The low cytotoxicity and good biocompatibility suggest that the FA-AuGds can act as promising multimodal contrast agents for cancer diagnosis.

### 3.4 *In vitro* and *in vivo* fluorescence imaging

To demonstrate the effectiveness of the FA-AuGds in *in vivo* tumor imaging of animals, the KB cells were used to establish a xenografted tumor model. The effectiveness of the NCs for targeted tumor imaging was also investigated *via* optical imaging in the first place. To choose the optimal observation time window, the time dependent distribution profiles of FA-AuGds in KB-tumor bearing mice were studied by measuring the Au concentration *via* ICP-MS (ESI Fig. S5†). Data indicated that the maximum uptake of AuGds in the tumor occurred at 4 h post tail vein injection. To facilitate the whole body real-time *in vivo* imaging, real-time images were acquired and analyzed for the time point 4 h post-injection. Saline injected mice were used as controls. As shown in Fig. 6a and b, 4 h after the AuGds and FA-AuGds were intravenously injected into the tail veins of the mice, fluorescence emissions could easily be detected from the whole of the body of the mice in a prone or lateral decubitus position. However, no fluorescence emissions were detectable from the bodies of the

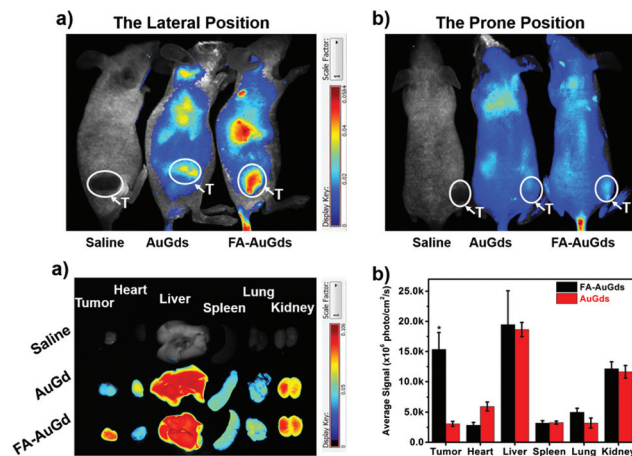


**Fig. 6** *In vivo* fluorescence imaging of KB tumor mice imaged 4 h after the tail vein injection. (a) Lateral position; (b) prone position. The mice from left to right correspond to saline, AuGd, and FA-AuGd injections. The white curve marks the boundaries of the tumor (T). (c) The *ex vivo* fluorescence of different organs taken after the *in vivo* imaging. (d) The average signal intensity of corresponding organs and tumor tissue from the mice injected with FA-AuGds (black bar) and AuGds (red bar). Each column represents the mean value ( $N = 3$ ) (asterisk (\*) denotes statistical significance. \*,  $p < 0.05$ ).

control mice. A comparison of the mice injected with AuGds with the mice injected with FA-AuGds reveals that the tumor site shows brighter fluorescence emissions in the mouse injected with FA-AuGds. The results indicate that the FA-AuGds have higher accumulation in the tumor than the AuGds. To directly observe the distribution of the nanoparticles, the mice were sacrificed after the whole body imaging, and *ex vivo* images of the liver, heart, spleen, lungs, kidneys, and tumor were compared (Fig. 6c and d). We found that the fluorescence intensities of the liver and kidney were much higher than those of other organs. This illustrates that both AuGds and FA-AuGds mainly accumulate in the liver and kidneys. However, there were some differences in the heart, lungs, and tumor, the mice injected with AuGds showed a stronger fluorescence emission in the heart than the mice injected with FA-AuGds; the opposite result was found for the lung. The tumor fluorescence imaging results were in good accord with the whole body real-time *in vivo* imaging. The average signal intensity of the tumor site directly indicated that more FA-AuGds than AuGds accumulated in the tumor site (Fig. 6d). In conclusion, the FA-AuGds show a good tumor targeting ability.

### 3.5 The $r_1$ relaxivity measurement and $T_1$ -weighted MRI *in vivo*

Gd-based materials are known to be good candidates for  $T_1$ -weighted MRI contrast agents. To evaluate the MR contrast ability of AuGds, the clinical MR contrast agent Gd-DTPA was chosen for comparisons with AuGds. The relaxation times of AuGds and Gd-DTPA were measured with a 7-T MR scanner. Fig. 7a shows the  $T_1$ -weighted MR phantom images of AuGds

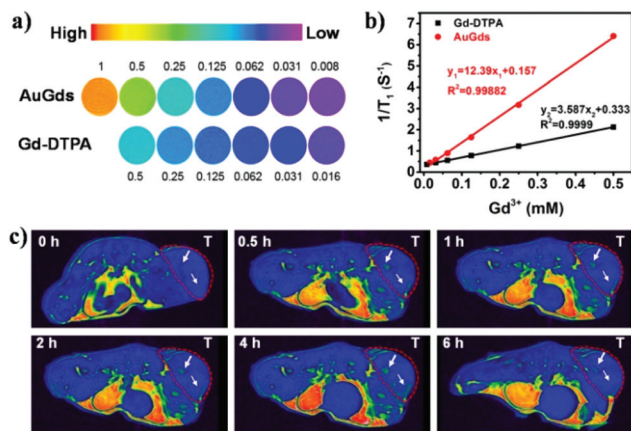


**Fig. 7** (a)  $T_1$ -Weighted MR phantom images of FA-AuGds and Gd-DTPA at various concentrations (mM). (b)  $r_1$  relaxivity curves for FA-AuGds and Gd-DTPA. (c) The transverse plane of the  $T_1$ -weighted 7-T MR images of KB tumor-bearing mice at 0, 0.5, 1, 2, 4, and 6 h after intravenous injection of FA-AuGds through the tail vein. The red dashed curve marks the boundaries of the tumor (T).

and Gd-DTPA with different concentrations of Gd. The signal increases with increasing Gd concentration, with the slope of  $1/T_1$  values vs. concentration (Fig. 7b) for AuGds (12.39) being much steeper than that of Gd-DTPA (3.58). The results indicate that the AuGds can be used as an efficient  $T_1$  contrast agent.

To confirm the  $T_1$ -weighted MRI ability of FA-AuGds, *in vivo* MRI was performed with a 7-T scanner using KB tumor bearing mice. Fig. 7c shows the  $T_1$ -weighted MR images of mice taken at 0, 0.5, 1, 2, 4, and 6 h post-injection. Fig. 7c demonstrates enhanced contrast and a brighter signal in the tumor bearing than in the control mouse (the same mouse without injecting NC particles), starting from 0.5 h post-injection. The images showed the greatest detail of the tumor structure at 4 h post-injection, with the tumor site having the brightest signal at this post-injection time. To quantitatively evaluate signal changes at the tumor site, specific regions were chosen for CNR measurements. The results presented in ESI Fig. S6† demonstrate a substantial increase in the CNR of region 1, with the maximum CNR appearing at 4 h. Similar results were found for region 2, indicating that the FA-AuGds efficiently accumulated in the tumor, reaching the greatest accumulation at 4 h post-injection. In summary, the data suggest that FA-AuGds could be used as  $T_1$  contrast agents for *in vivo* MR imaging of tumors.

### 3.6 Hounsfield unit (HU) values and *in vivo* CT tumor imaging

On the basis of the X-ray absorption coefficient rule, both Au and Gd are high atomic number ( $Z$ ) elements, and can serve as CT contrast agents.<sup>35,36</sup> To demonstrate the CT imaging ability of AuGds, the HU values were measured for the same Au concentration intervals for the Au cluster NCs and AuGd solution. The commercial iodine-based contrast agent iopromide (Ultravist 300, Schering, Berlin, Germany) was selected for

comparison with the AuGds. As seen from Fig. 8a, the phantom images of all the agents increased in brightness with increasing concentration of Au or I. AuGds and Au clusters (Au = 40 mM) had comparable brightness to iopromide (I = 100 mM). To quantify the signal changes, we plotted the HU value against the Au or I concentration. As shown in Fig. 8b, at 40 mM Au or I element concentration, the HU value of AuGds (approximately 700 HU) was higher than that of Au clusters (~500 HU) and iopromide (~200 HU). This demonstrated that Gd promoted the HU value of the AuGds in comparison to the Au clusters with the same Au concentration. The slope of HU values vs. concentration (Fig. 8b) of AuGds (15.98) is almost 3 times higher than that of iopromide (4.79), which shows promising potential of the AuGds as CT imaging agents.

As shown in the *in vivo* CT imaging of FA-AuGds (Fig. 8c), the FA-AuGds were mainly located in the liver, kidney, and spleen at 4 h post-intravenous injection. Their extraction from the body occurred through urine, with part of the FA-AuGds still being visible in the bladder. These results are consistent with the optical images; however, a substantial difference is that the tumor could not be delineated by CT with the same FA-AuGd injection dose used for optical imaging. This was because of the limited sensitivity of CT. To carry out tumor imaging, 20  $\mu$ l of FA-AuGds were directly injected into the KB tumor, and an image was taken 30 min post-injection. As a result of this injection, the tumor site showed an obvious enhancement of the CT signal at the edge of the tumor and in

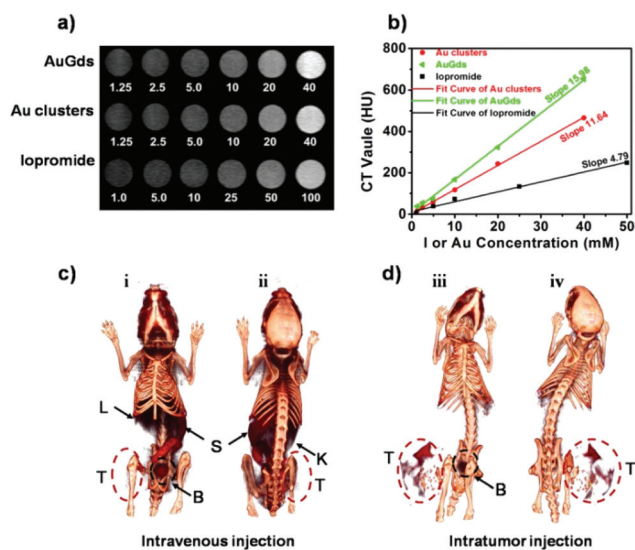


**Fig. 8** (a) CT phantom images of AuGds, Au clusters and iopromide with different elemental concentrations (Au: 1.25, 2.5, 5.0, 10, 20, 40 mM; I: 1.0, 5.0, 10, 25, 50, 100 mM). (b) HU values at different Au and I concentrations. (c–d) *In vivo* CT imaging of KB tumor-bearing mice at (c) 4 h post-intravenous injection, and (d) 30 min post-intratumor injection of FA-AuGds. Supine position view of mice: i and iii; prone position: ii and iv. The dashed curves mark the position of the bladder (B) and tumor (T), and the arrows indicate the position of the kidney (K), liver (L) and spleen (S).

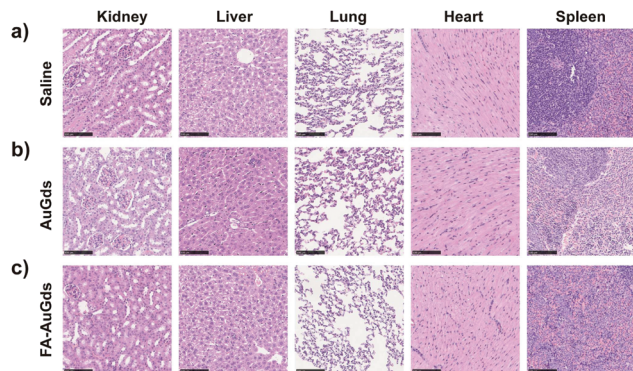


**Fig. 9** Histological changes in the heart, liver, spleen, lung, and kidney of mice injected with the different nanoparticles after one week. (a) Saline injected; (b) AuGds injected; (c) FA-AuGds injected. Scale bar: 100  $\mu$ m.

the intra-tumoral veins. We also noticed the extraction of FA-AuGds *via* the urine.

### 3.7 Pathology test of FA-AuGds and AuGds in mice

To investigate the potential toxicity of the FA-AuGds and AuGds *in vivo*, histological changes in several susceptible organs, including the heart, liver, spleen, lungs, and kidneys were investigated. High doses of FA-AuGd and AuGds were intravenously injected into the tails of the mice. One week after the I.V. injection, the mice were sacrificed, and the organs were stained with hematoxylin and eosin (H&E), and then observed under a light microscope. The results showed no obvious histological change compared with the saline injected mice (Fig. 9). These preliminary results show that FA-AuGds and AuGds exhibit good short-term biocompatibility at the tested dosage.

## 4. Conclusions

In summary, we successfully constructed an optical/CT/MR triple-modal nanoprobe for targeted tumor imaging *in vivo*. We accomplished this through a one-step bio-mineralization method using BSA as a template. When the integrated triple-modal imaging agent AuGds was functionalized with FA, the FA-AuGds could specifically target folate receptor over-expressing KB cells, and showed no cytotoxicity. The FA-AuGds are stable in 10% FBS buffer for 24 h. Comparisons of FA-AuGds with Gd-DTPA and iopromide demonstrated that the triple-modal probe had improved MR and CT signals. Triple-modal optical, MR, and CT imaging of KB tumor-bearing mice was achieved by tail vein injection. The FA-AuGd probe has good biocompatibility, is quickly excreted *via* renal clearance, and does not demonstrate any tissue toxicity *in vivo*. Therefore, FA-AuGds can be considered as novel candidates for targeted tumor imaging for future medical diagnoses.

## Acknowledgements

This work was financially supported by the National Key Basic Research Program of China (2013CB932703) and the National Natural Science Foundation of China (21390414, 21425522, 21675157, 11535015, 31271072, 31300827).

## Notes and references

- R. L. Siegel, K. D. Miller and A. Jemal, *CA-Cancer J. Clin.*, 2015, **65**, 5–29.
- T. Persigehl, J. Ring, C. Bremer, W. Heindel, R. Holtmeier, J. Stypmann, M. Claesener, S. Hermann, M. Schäfers, C. Zerbst, C. Schliemann, R. M. Mesters, W. E. Berdel and C. Schwöppe, *Angiogenesis*, 2014, **17**, 235–246.
- D. E. Lee, H. Koo, I. C. Sun, J. H. Ryu, K. Kim and I. C. Kwon, *Chem. Soc. Rev.*, 2012, **41**, 2656–2672.
- A. Signore, S. J. Mather, G. Piaggio, G. Malviya and R. A. Dierckx, *Chem. Rev.*, 2010, **110**, 3112–3145.
- B. Zhou, L. Zheng, C. Peng, D. Li, J. Li, S. Wen, M. Shen, G. Zhang and X. Shi, *ACS Appl. Mater. Interfaces*, 2014, **6**, 17190–17199.
- J. Zhou, Z. Lu, G. Shan, S. Wang and Y. Liao, *Biomaterials*, 2014, **35**, 368–377.
- T. Nam, S. Park, S. Y. Lee, K. Park, K. Choi, I. C. Song, M. H. Han, J. J. Leary, S. A. Yuk, I. C. Kwon, K. Kim and S. Y. Jeong, *Bioconjugate Chem.*, 2010, **21**, 578–582.
- V. S. Harrison, C. E. Carney, K. W. Macrenaris and T. J. Meade, *Chem. Commun.*, 2014, **50**, 11469–11471.
- S. Chen, Y. Yang, H. Li, X. Zhou and M. Liu, *Chem. Commun.*, 2014, **50**, 283–285.
- D. Vonwil, J. Christensen, S. Fischer, O. Ronneberger and V. P. Shastri, *Mol. Imaging Biol.*, 2014, **16**, 350.
- L. Lu, X. Wang, C. Xiong and L. Yao, *Sci. China: Chem.*, 2015, **58**, 793–809.
- W. He, K. Ai and L. Lu, *Sci. China: Chem.*, 2015, **58**, 753–760.
- R. Popovtzer, A. Agrawal, N. A. Kotov, A. Popovtzer, J. Balter, T. E. Carey and R. Kopelman, *Nano Lett.*, 2008, **8**, 4593–4596.
- D. Ma, L. Meng, Y. Chen, M. Hu, Y. Chen, C. Huang, J. Shang, R. Wang, Y. Guo and J. Yang, *ACS Appl. Mater. Interfaces*, 2015, **7**, 16257–16265.
- J. V. Jokerst and S. S. Gambhir, *Acc. Chem. Res.*, 2011, **44**, 1050–1060.
- K. Chaudhari, P. L. Xavier and T. Pradeep, *ACS Nano*, 2011, **5**, 8816–8827.
- A. Retnakumari, S. Setua, D. Menon, P. Ravindran, H. Muhammed, T. Pradeep, S. Nair and M. Koyakutty, *Nanotechnology*, 2010, **21**, 055103.
- Y. Wang, Y. Cui, R. Liu, F. Gao, L. Gao and X. Gao, *Sci. China: Chem.*, 2015, **58**, 1–6.
- L. Jing, X. Liang, Z. Deng, S. Feng, X. Li, M. Huang, C. Li and Z. Dai, *Biomaterials*, 2014, **35**, 5814–5821.

- 20 C. Zhang, Z. Zhou, Q. Qian, G. Gao, C. Li, L. Feng, Q. Wang and D. Cui, *J. Mater. Chem.*, 2013, **1**, 5045–5053.
- 21 A. Samanta, B. B. Dhar and R. N. Devi, *J. Phys. Chem. C*, 2012, **116**, 1748–1754.
- 22 X. Wu, X. He, K. Wang, C. Xie, B. Zhou and Z. Qing, *Nanoscale*, 2010, **2**, 2244–2249.
- 23 Y. Wang, C. Xu, J. Zhai, F. Gao, R. Liu, L. Gao, Y. Zhao, Z. Chai and X. Gao, *Anal. Chem.*, 2015, **87**, 343–345.
- 24 J. L. Bridot, A. C. Faure, S. Laurent, C. Riviere, C. Billotey, B. Hiba, M. Janier, V. Josserand, J. L. Coll, L. V. Elst, R. Muller, S. Roux, P. Perriat and O. Tillement, *J. Am. Chem. Soc.*, 2007, **129**, 5076–5084.
- 25 M. Ahren, L. Selegard, A. Klasson, F. Soderlind, N. Abrikosova, C. Skoglund, T. Bengtsson, M. Engström, P. O. Käll and K. Uvdal, *Langmuir*, 2010, **26**, 5753–5762.
- 26 J. Li, J. You, Y. Dai, M. Shi, C. Han and K. Xu, *Anal. Chem.*, 2014, **86**, 11306–11311.
- 27 J. Xie, J. Y. Lee, D. I. C. Wang and Y. P. Ting, *ACS Nano*, 2007, **1**, 429–439.
- 28 C. Tanford and G. L. Roberts, *J. Am. Chem. Soc.*, 1952, **74**, 2509–2514.
- 29 J. Xie, Y. Zheng and J. Y. Ying, *J. Am. Chem. Soc.*, 2009, **131**, 888–889.
- 30 S. K. Sun, L. X. Dong, Y. Cao, H. R. Sun and X. P. Yan, *Anal. Chem.*, 2013, **85**, 8436–8441.
- 31 A. T. Anishur Rahman, K. Vasilev and P. Majewski, *J. Colloid Interface Sci.*, 2011, **354**, 592–596.
- 32 N. Chen, C. Shao, Y. Qu, S. Li, W. Gu, T. Zheng, L. Ye and C. Yu, *ACS Appl. Mater. Interfaces*, 2014, **6**, 19850–19857.
- 33 E. J. De, J. J. Keating, S. A. Kularatne, J. Jiang, R. Judy, J. Predina, S. Nie, P. Low and S. Singhal, *Int. J. Mol. Imaging*, 2015, **2015**, 469047.
- 34 F. Gao, Y. Lin, L. Li, Y. Liu, U. Mayerhöffer, P. Spent, J. Su, J. Li, F. Würthner and H. Wang, *Biomaterials*, 2014, **35**, 1004–1014.
- 35 Y. Liu, K. Ai and L. Lu, *Acc. Chem. Res.*, 2012, **45**, 1817–1827.
- 36 H. Lusic and M. W. Grinstaff, *Chem. Rev.*, 2013, **113**, 1641–1666.